Supporting Information for

Layers and Phase Identification of h- and m-GaTe via Second Harmonic Generation

Shi Qiu,[a,b] Hongsheng Liu,[b] Juan Hou,[a] Zhongran Wei,[a,*] Hu Jiang,[a,*] and Junfeng Gao[b,*]

[a] College of Sciences/State Key Laboratory of Advanced Energy Storage Materials and Technology, Shihezi University, Xinjiang, Shihezi, 832003, China

[b] Key Laboratory of Materials Modification by Laser, Ion and Electron Beams (Dalian University of Technology), Ministry of Education, School of Physics, Dalian 116024, China

1 Methods

Ground-state crystal structures GaTe ware calculated by first-principles density-functional theory (DFT)[1] implemented in the Vienna Ab initio Simulation Package (VASP)[2] with a plane-wave basis and the projector-augmented wave method.[3] Here we used the Perdew–Burke–Ernzerhof (PBE)[4] exchange-correlation functional within the generalized-gradient approximation (GGA)[5] and a Γ-centered k-point sampling for the Brillouin zone (BZ) integration. An energy cutoff of 450 eV for the plane-wave basis and a Γ-centered k-point scheme with k-mesh-resolved value of $0.03 \times 2\pi$ $^{-1}$ for the geometry optimization calculation, and $0.015 \times 2\pi$ $^{-1}$ for the electronic structure calculation were adopted. The convergence criterion of total energy was set to 10^{-7} eV. The geometry optimization was considered to be successful when the residual force on each atom was less than 0.01 eV^{-1}. To avoid the interactions between adjacent layers, a vacuum region of 15 was added in the vertical direction for two-dimensional crystals. Since the conventional GGA functional like PBE tends to underestimate the band gaps, a hybrid functional (HSE06)[6] was used to compute the electronic structures.

In order to discuss the light absorption capacity of the material, the linear optical response is directly related to the complex dielectric function $\varepsilon(\omega) = \varepsilon_1(\omega) + i\varepsilon_2(\omega)$. The imaginary part of the dielectric function $\varepsilon_2(\omega)$ is given by

$$\varepsilon_2^{ab}(\omega) = \int \frac{dk}{4\pi^3} \sum_{nm} f_{nm} \frac{r_{nm}^a r_{mn}^b}{\omega_{nm} - \omega}, \tag{1}$$

where $f_{nm} = f_n - f_m$ and $\omega_{nm} = \omega_n - \omega_m$ are the Fermi distribution function difference and the energy (frequency) difference between the n-th and m-th bands, respectively. r_{nm} is the position operator obtained by $r_{nm} = p_{nm}/(im_e\omega_{nm})$. The real part of the dielectric function can be obtained from the imaginary one by Kramers–Kronig[7,8] transformation. All other linear optical properties, including refractive index, birefringence, reflectivity, and absorption spectrum can be derived by using the dielectric function.

The SHG susceptibility $\chi^{(2)}(-2\omega, \omega, \omega)$ tensor is computed within the independent-particle approximation[9,10] using a self-developed highly efficient, parallel code based on VASP output files. At present, Fortran 90 and Python 3.10 versions of the code have been developed. Using Message Pass-

ing Interface (OpenMPI for Fortran and mpi4py for Python) and parallel computations on k-points, excellent parallelization performance can be maintained for up to a few thousand processors. This development enables us to calculate large-scale systems with low symmetry.

The SHG can be divided into two types: one is in the zero-frequency limit, and the other is frequency-dependent. The SHG tensor at the zero-frequency limit is expressed as[11]

$$\chi^{abc}_{zero} = \chi^{abc}_{e} + \chi^{abc}_{i}, \tag{2}$$

where χ^{abc}_{e} is the contribution of purely interband processes and χ^{abc}_{i} is the contribution of mixed interband and intraband processes. They are given by

$$\chi^{abc}_{e} = \frac{e^3}{\hbar^2}\int \frac{d\mathbf{k}}{4\pi^3}\sum_{nml}\frac{r^a_{nm}\left\{r^b_{ml}r^c_{ln}\right\}}{\omega_{nm}\omega_{ml}\omega_{ln}}\left[\omega_n f_{ml}+\omega_m f_{ln}+\omega_l f_{nm}\right], \tag{3}$$

$$\begin{aligned}\chi^{abc}_{i} = \frac{i}{4}\frac{e^3}{\hbar^2}\int \frac{d\mathbf{k}}{4\pi^3}\sum_{nm}\frac{f_{nm}}{\omega^2_{mn}}\Big[&r^a_{nm}\left(r^b_{mn;c}+r^c_{mn;b}\right)\\ &+r^b_{nm}\left(r^a_{mn;c}+r^c_{mn;a}\right)+r^c_{nm}\left(r^a_{mn;b}+r^b_{mn;a}\right)\Big],\end{aligned} \tag{4}$$

and

$$\left(r^b_{nm}\right)_{;\mathbf{k}^a} = \frac{r^a_{nm}\Delta^b_{mn}+r^b_{nm}\Delta^a_{mn}}{\omega_{nm}}+\frac{i}{\omega_{nm}}\sum_l\left(\omega_{lm}r^a_{nl}r^b_{lm}-\omega_{nl}r^b_{nl}r^a_{lm}\right), \tag{5}$$

where $\Delta_{nm}=V_n-V_m$ is the electron group velocity difference between the n-th and m-th bands, and $\{r^b_{ml}r^c_{ln}\}$ is defined as $\frac{1}{2}(r^b_{ml}r^c_{ln}+r^c_{ml}r^b_{ln})$. Here e is the electron charge and $\hbar$ is the reduced Planck constant.

The frequency-dependent SHG tensor can be expressed as[12]

$$\chi^{abc}_{\text{total}} = \chi^{abc}_{\text{inter}} + \chi^{abc}_{\text{intra}} + \chi^{abc}_{\text{mod}}. \tag{6}$$

The $\chi^{abc}_{\text{inter}}$ term is the purely interband contribution. The $\chi^{abc}_{\text{intra}}$ term is the purely intraband contribution from electrons and the χ^{abc}_{mod} term represents the effect of interband transitions on the intraband

contribution. Thus $\chi^{abc}_{\text{intra}} + \chi^{abc}_{\text{mod}}$ is the total intraband contribution. They are given by

$$\chi^{abc}_{\text{inter}}(2\omega,\omega,\omega) = \frac{e^3}{\hbar^2}\sum_{nml}{}' \int \frac{d\mathbf{k}}{4\pi^3} \frac{r^a_{nm}\{r^b_{ml}r^c_{ln}\}}{(\omega_{ln}-\omega_{ml})} \left\{ \frac{2f_{nm}}{\omega_{mn}-2\omega} + \frac{f_{ml}}{\omega_{ml}-\omega} + \frac{f_{ln}}{\omega_{ln}-\omega} \right\}, \tag{7}$$

$$\begin{aligned} \chi^{abc}_{\text{intra}}(2\omega,\omega,\omega) = {} & \frac{e^3}{\hbar^2}\int \frac{d\mathbf{k}}{4\pi^3} \left[\sum_{nml}{}' \omega^a_{mn} r^a_{nm}\{r^b_{ml}r^c_{ln}\} \left\{ \frac{f_{nl}}{\omega^2_{ln}(\omega_{ln}-\omega)} - \frac{f_{lm}}{\omega^2_{ml}(\omega_{ml}-\omega)} \right\} \right. \\ & \left. -8i\sum_{nm}{}' \frac{f_{nm} r^a_{nm}\{\Delta^b_{mn} r^c_{mn}\}}{\omega^2_{mn}(\omega_{mn}-2\omega)} + 2\sum_{nml}{}' \frac{f_{nm} r^a_{nm}\{r^b_{ml}r^c_{ln}\}(\omega_{ml}-\omega_{ln})}{\omega^2_{mn}(\omega_{mn}-2\omega)} \right], \end{aligned} \tag{8}$$

$$\begin{aligned} \chi^{abc}_{\text{mod}}(2\omega,\omega,\omega) = {} & \frac{e^3}{2\hbar^2}\int \frac{d\mathbf{k}}{4\pi^3} \left[\sum_{nml}{}' \frac{f_{nm}}{\omega^2_{mn}(\omega_{mn}-\omega)} \{\omega_{nl} r^a_{lm}\{r^b_{mn}r^c_{nl}\} \right. \\ & \left. -\omega_{lm} r^a_{nl}\{r^b_{lm}r^c_{mn}\}\} - i\sum_{nm}{}' \frac{f_{nm} r^a_{nm}\{r^b_{mn}\Delta^c_{mn}\}}{\omega^2_{mn}(\omega_{mn}-\omega)} \right]. \end{aligned} \tag{9}$$

We now focus on the matrix elements of the momentum operator in Bloch waves. Within the PAW formalism, the momentum operator matrix element is given by

$$\langle \psi_{c\mathbf{k}} | \mathbf{p} | \psi_{v\mathbf{k}} \rangle = \hbar \langle u_{c,\mathbf{k}} | \mathbf{k} - i\nabla | u_{v,\mathbf{k}} \rangle, \tag{10}$$

which can be evaluated from the pseudo-wavefunctions calculated by VASP.

Since the calculation of optical properties based on the above equations necessitates precise electronic structure, including accurate band structures and momentum matrix elements p_{nm}, a large number of bands and dense k-meshes are required. Over 100 conduction bands were used to obtain converged SHG susceptibility tensors. The issue of formula divergence is addressed by introducing a small positive imaginary part in the frequency.[13] Considering the underestimation of the energy band gap by PBE/GGA in optical property calculations, we employ the scissor approximation[14] and utilize the HSE06 functional to obtain a more accurate correction for the gap. Furthermore, given the uncertain thickness of the two-dimensional material, it is necessary to renormalize the SHG susceptibility. In order to ensure the consistency of units, we adopt

$$\chi^{\text{SHG}}_{\text{sheet}} = \chi^{\text{SHG}}_{\text{bulk}} \times \frac{L_z}{d},$$

where d is the 2D layer thickness, which is assumed as the vertical coordinate distance between the outermost atomic planes plus a van der Waals distance of 3 , and L_z is the lattice length perpendicular to the sample plane. In this way, the unit of sheet SHG susceptibility is in pm/V.

2 The Atomic and Electronic Structure of Bulk GaTe

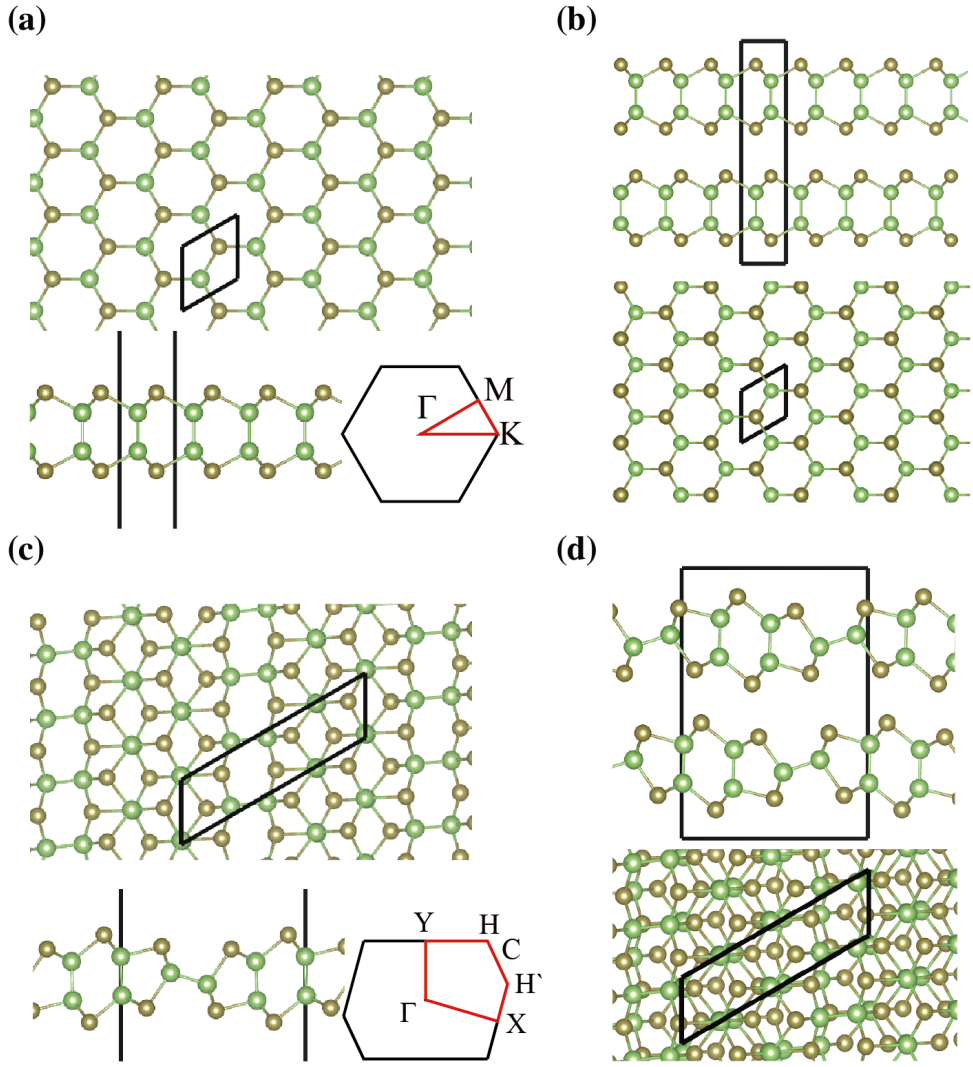

Fig. S1 Top (top) and side (bottom left) view of the atomic structures (Ga in green and Te in gold) and band structure loops in the first Brillouin zone (bottom right) of monolayer h- (a) and m-GaTe (c). Similar top (top) and side (bottom) views of the atomic structures of bulk h- (b) and m-GaTe (d).

The atomic structures of monolayer and bulk GaTe are shown in Fig. S1. Multilayer structures have been obtained by cleaving the corresponding bulk ones followed by subsequent optimization.

3 Electronic Structure and Optical Response of Multilayer GaTe

The electronic band structures of monolayer to pentlayer have been calculated at the PBE and HSE06 levels, as shown in Fig. S2 and Fig. S3.

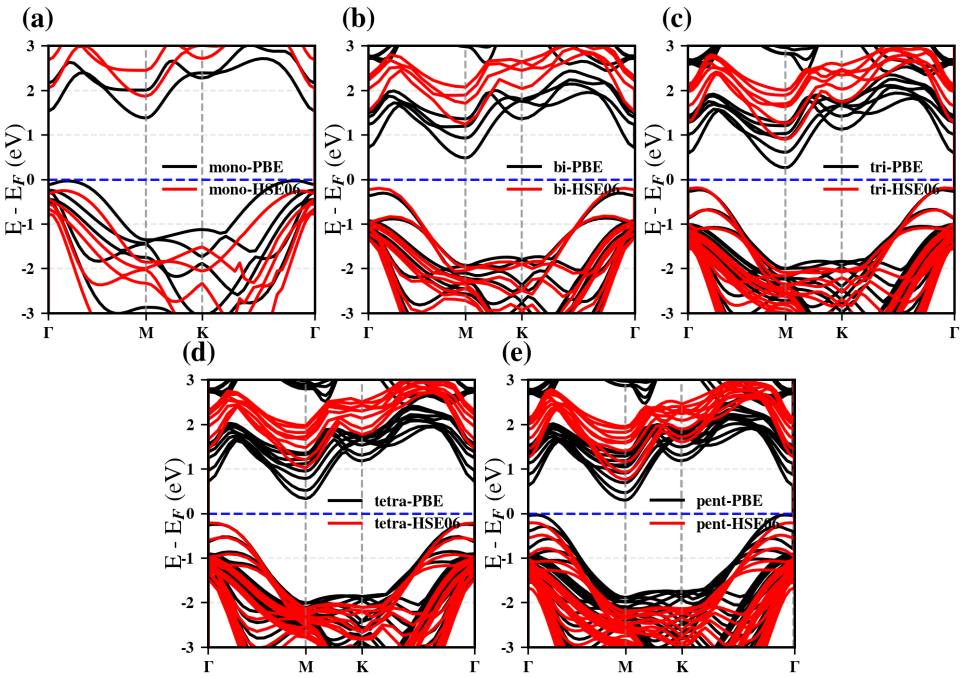

Fig. S2 Electronic band structures calculated by PBE (black lines) and HSE06 (red lines) for h-GaTe from monolayer to pentlayer. The Fermi level has been set as zero.

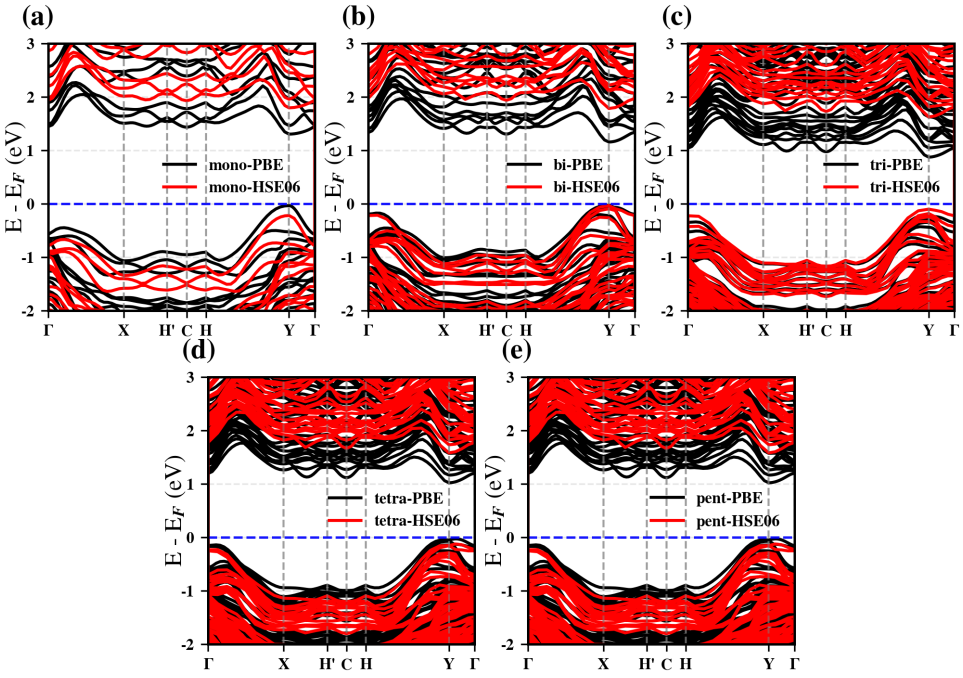

Fig. S3 Electronic band structures calculated by PBE (black lines) and HSE06 (red lines) for m-GaTe from monolayer to pentlayer. The Fermi level has been set as zero.

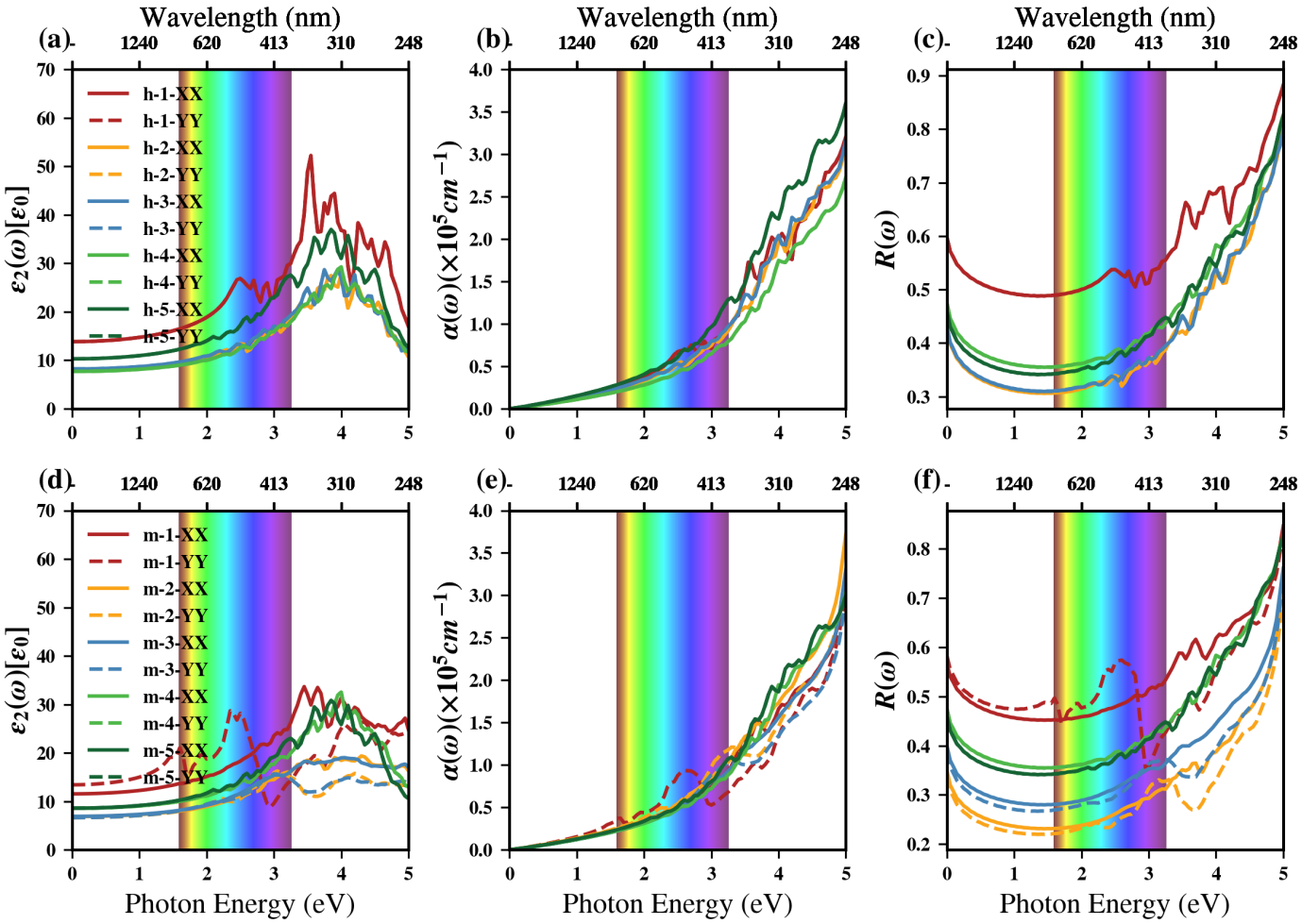

Fig. S4 Imaginary part of the dielectric function $\varepsilon_2(\omega)$ (a and d), absorption coefficient $\alpha(\omega)$(b and e) and reflectivity $R(\omega)$ (c and f) for multilayer GaTe. Panels (a – c) show h-GaTe and panels (d – f) show m-GaTe. The shaded region marks the visible–light range. Solid and dashed curves denote the in-plane xx and yy components, respectively. Color code: monolayer (red), bilayer (orange), trilayer (blue),tetralayer (light green) and pentalayer (green).

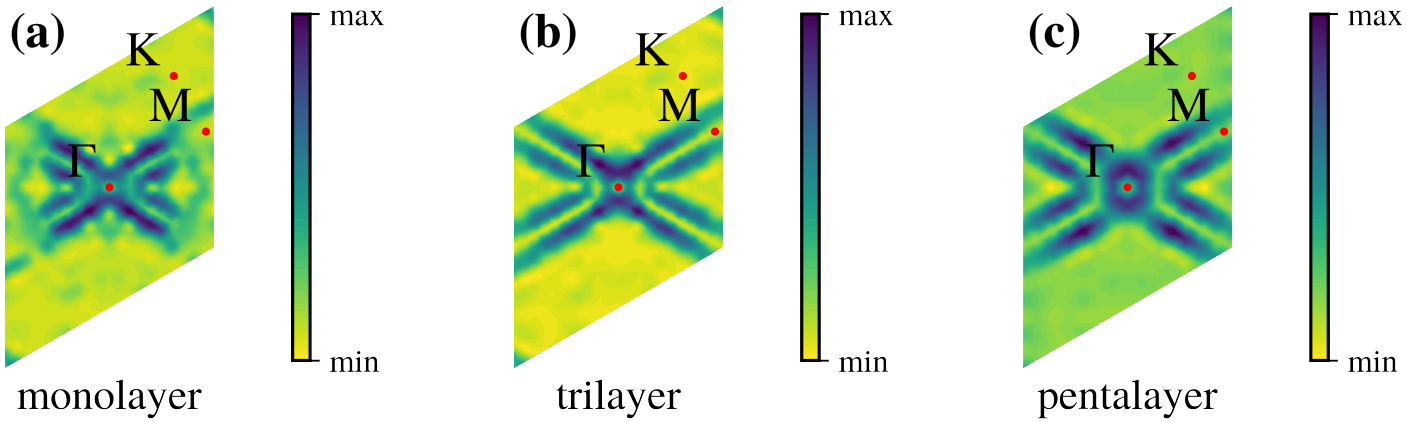

Fig. S5 In Whole Brillouin zone for monolayer (a), trilayer (b) and pentalayer (c) h-GaTe, k-pooints resolved SHG response strength near SHG peak of multilayer GaTe when the incident photon energy is 2.15 eV.

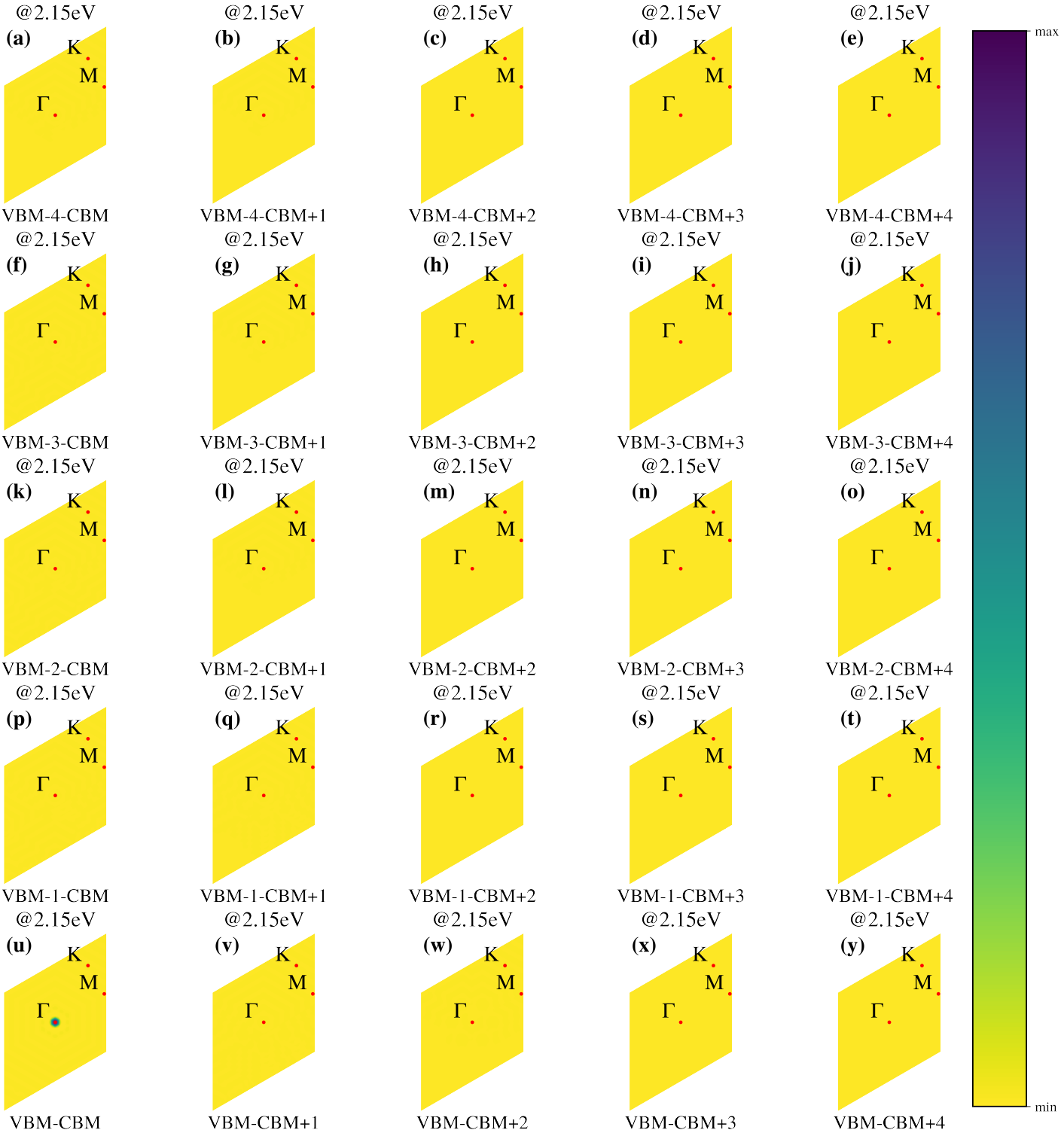

Fig. S6 *K*-resolved transition-matrix-element-weighted joint density of states (TM-JDOS) over the entire Brillouin zone of monolayer GaTe at an incident photon energy of 2.15 eV, resolved between different interband transitions. Red markers indicate the locations of high-symmetry k points.

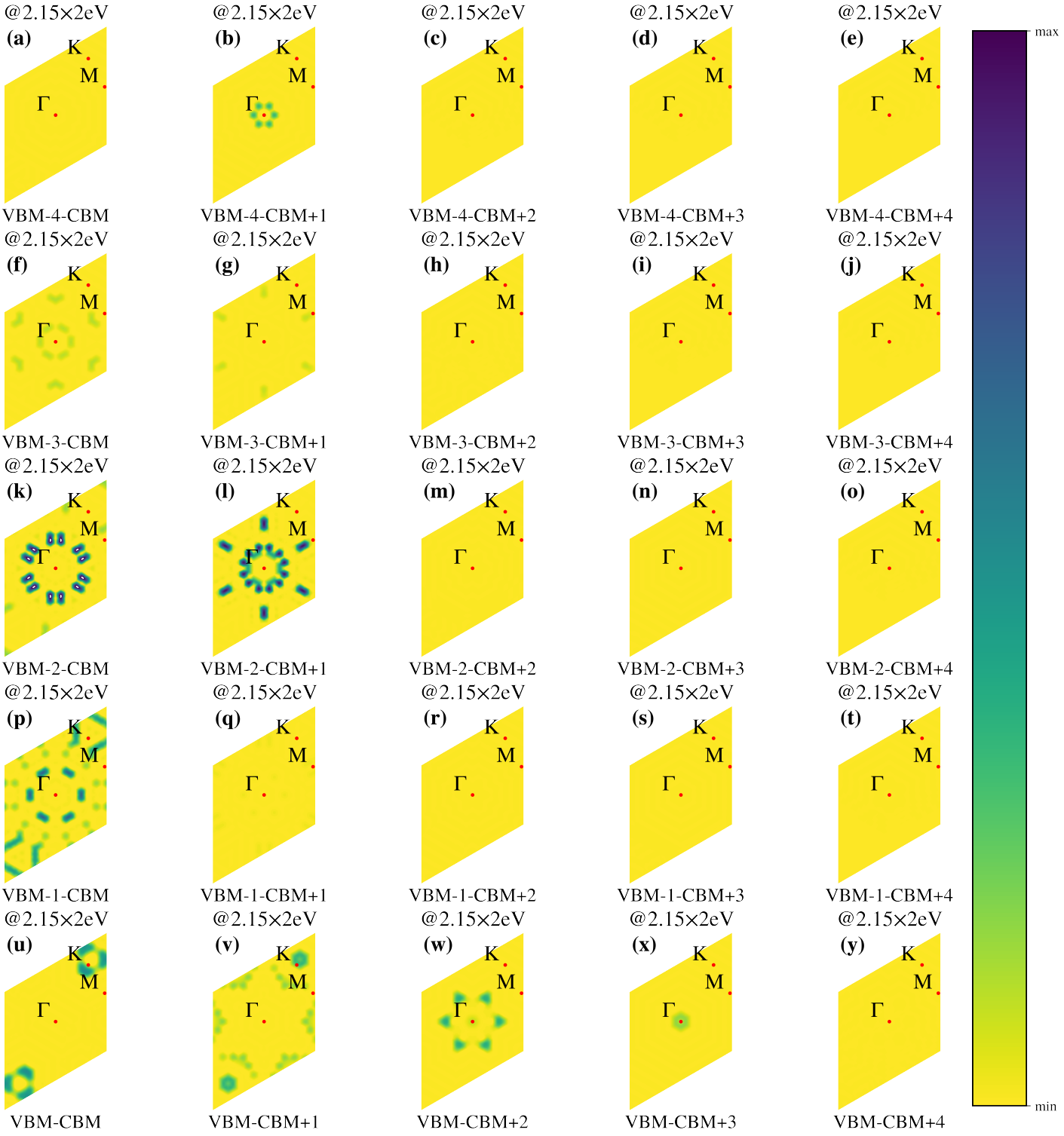

Fig. S7 *K*-resolved transition-matrix-element-weighted joint density of states (TM-JDOS) over the entire Brillouin zone of monolayer GaTe at an incident photon energy of 2.15×2 eV, resolved between different interband transitions. Red markers indicate the locations of high-symmetry k points.

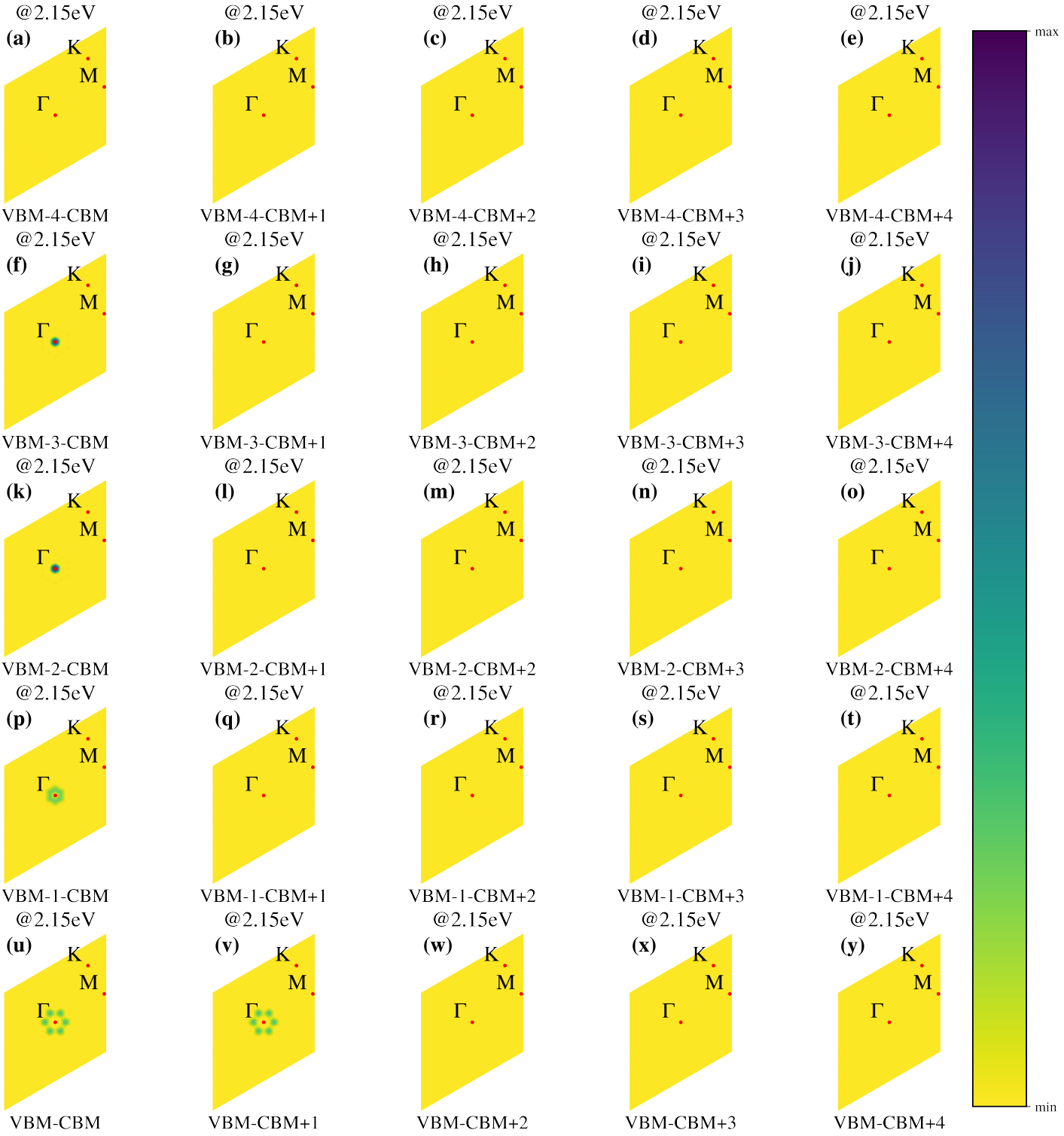

Fig. S8 *K*-resolved transition-matrix-element-weighted joint density of states (TM-JDOS) over the entire Brillouin zone of trilayer GaTe at an incident photon energy of 2.15 eV, resolved between different interband transitions. Red markers indicate the locations of high-symmetry k points.

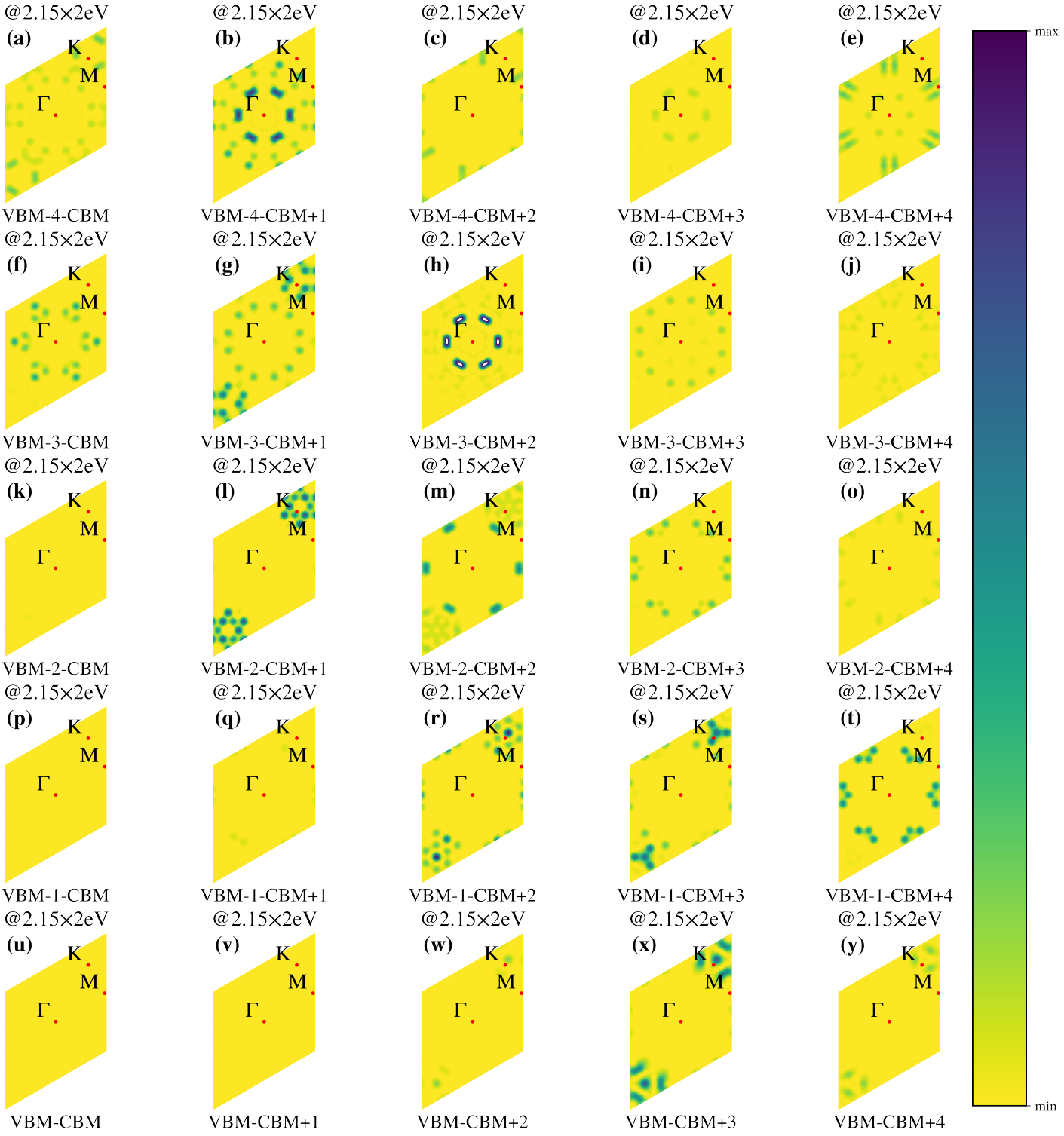

Fig. S9 K-resolved transition-matrix-element-weighted joint density of states (TM-JDOS) over the entire Brillouin zone of trilayer GaTe at an incident photon energy of 2.15×2 eV, resolved between different interband transitions. Red markers indicate the locations of high-symmetry k points.

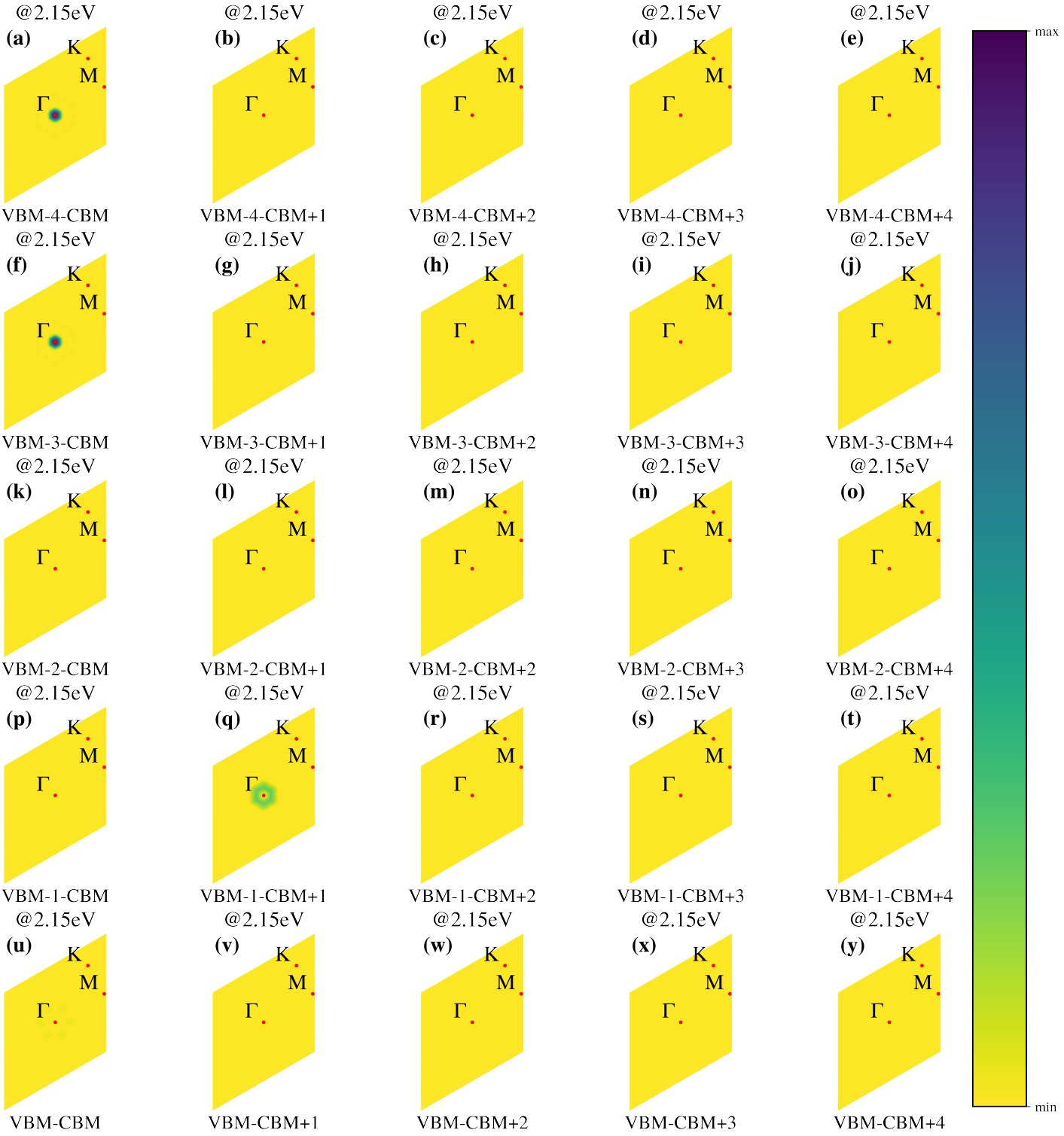

Fig. S10 *K*-resolved transition-matrix-element-weighted joint density of states (TM-JDOS) over the entire Brillouin zone of pentalayer GaTe at an incident photon energy of 2.15 eV, resolved between different interband transitions. Red markers indicate the locations of high-symmetry k points.

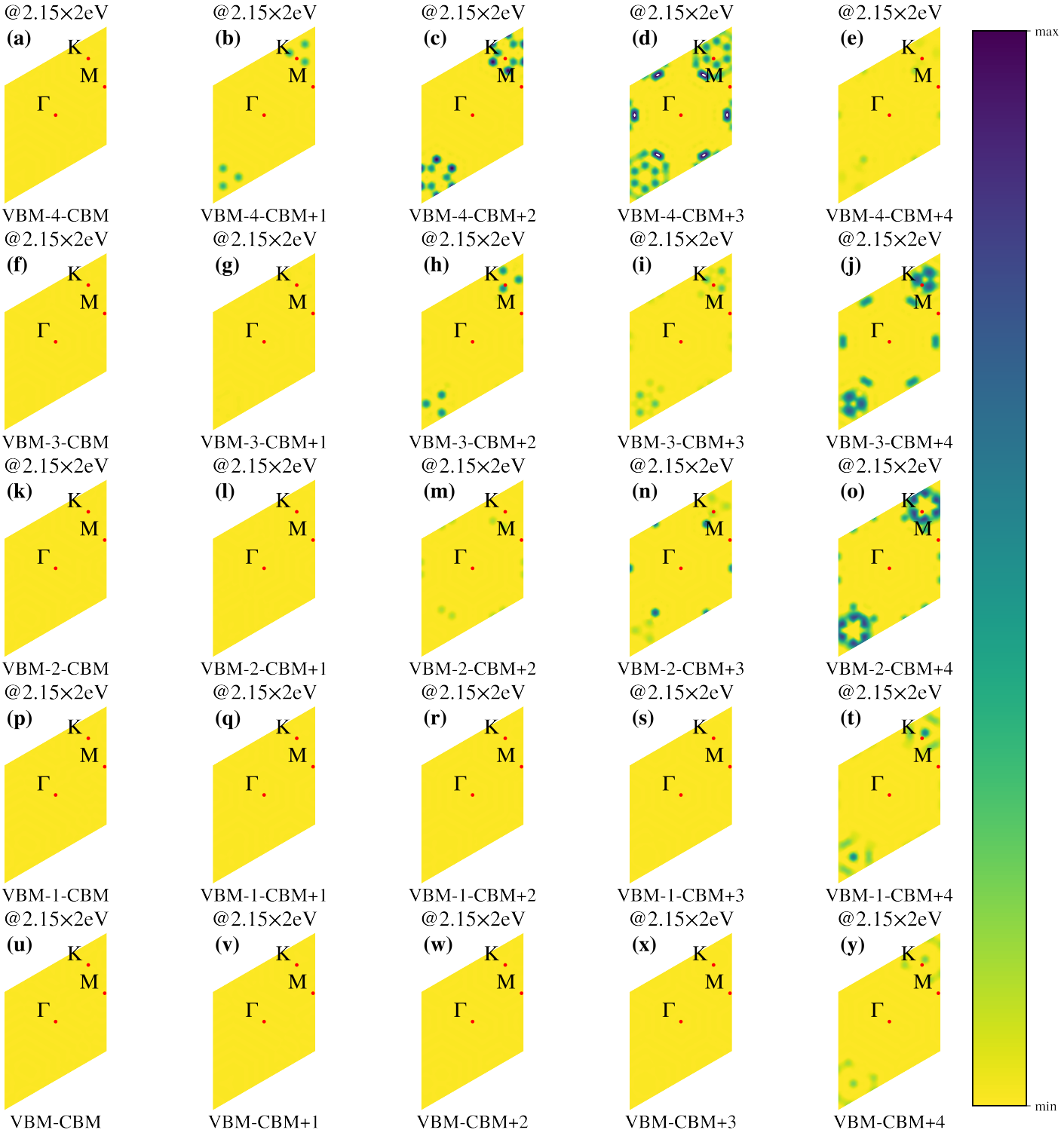

Fig. S11 *K*-resolved transition-matrix-element-weighted joint density of states (TM-JDOS) over the entire Brillouin zone of pentalayer GaTe at an incident photon energy of 2.15×2 eV, resolved between different interband transitions. Red markers indicate the locations of high-symmetry k points.

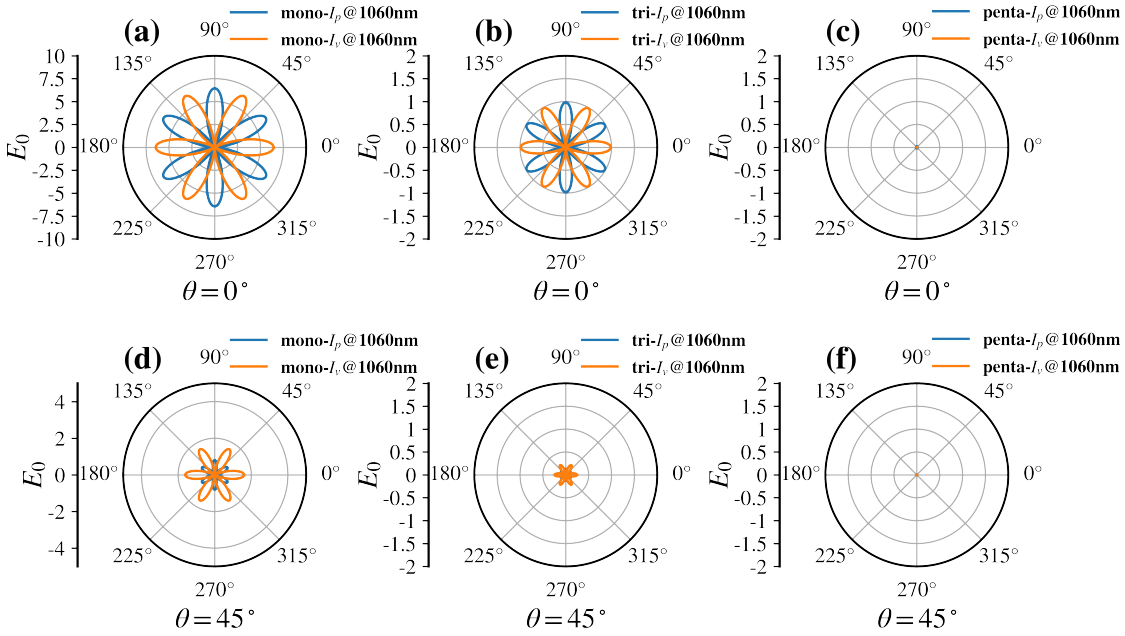

Fig. S12 Polar plots of the SHG intensity from monolayer (a and d), trilayer (b and e), and pentalayer (c and f) h-GaTe as a function of the azimuthal angle $\phi = 0^\circ$ or 45°. The blue (orange) lines denote the component of SHG response parallel (I_p)(prependicular (I_v)) to the polarization $E(\omega)$ of the incident light 1060 nm.

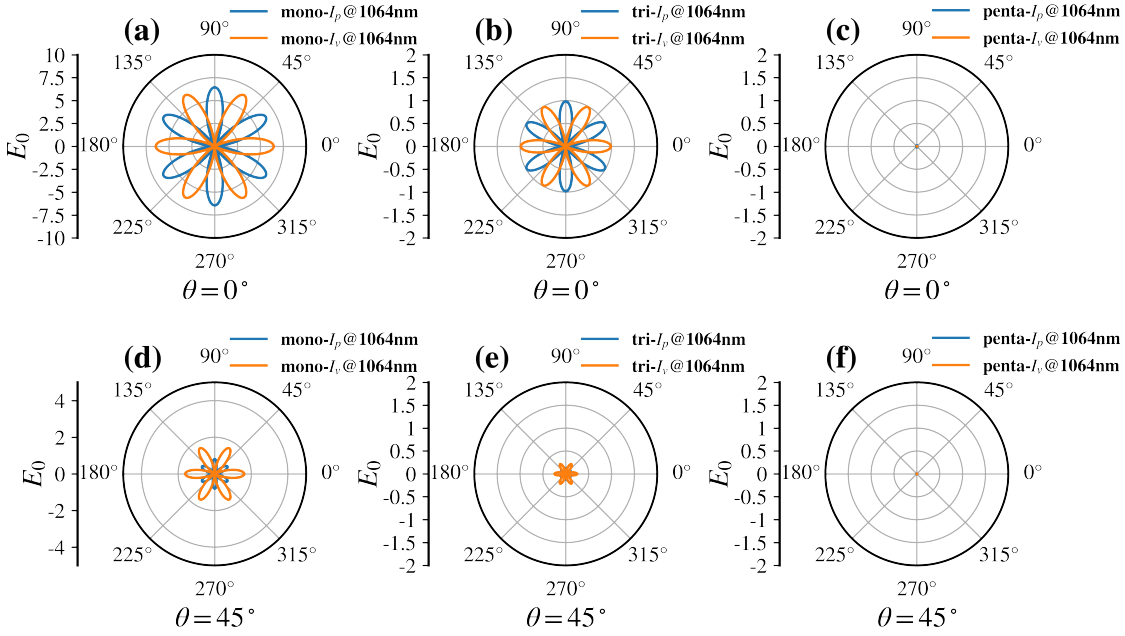

Fig. S13 Polar plots of the SHG intensity from monolayer (a and d), trilayer (b and e), and pentalayer (c and f) h-GaTe as a function of the azimuthal angle $\phi = 0^\circ$ or 45°. The blue (orange) lines denote the component of SHG response parallel (I_p)(prependicular (I_v)) to the polarization $E(\omega)$ of the incident light 1064 nm.

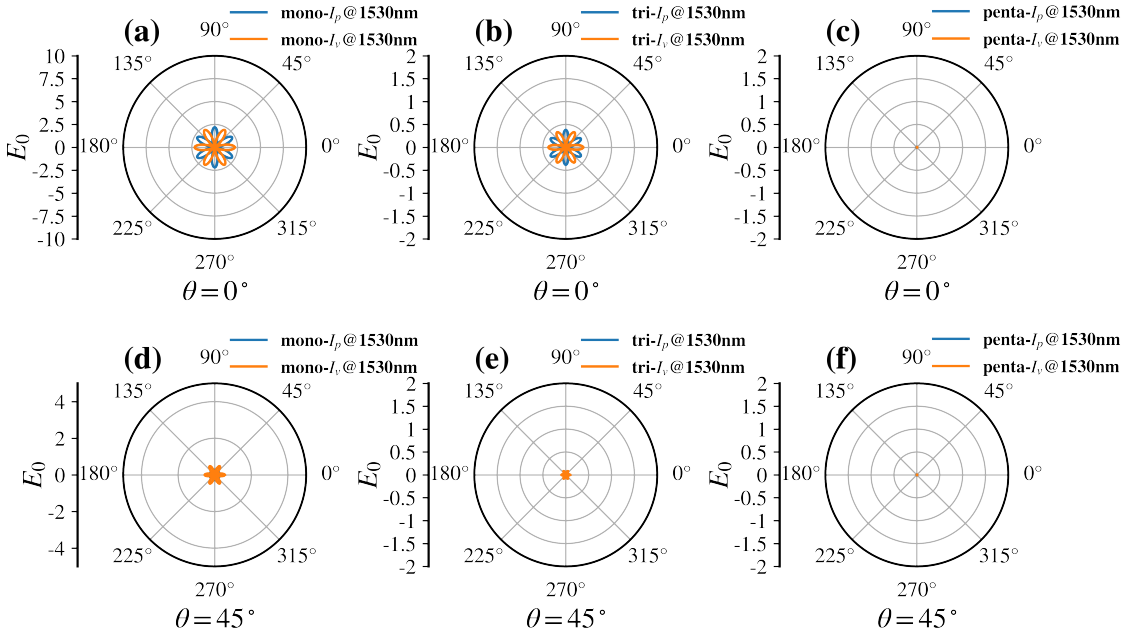

Fig. S14 Polar plots of the SHG intensity from monolayer (a and d), trilayer (b and e), and pentalayer (c and f) h-GaTe as a function of the azimuthal angle $\phi = 0^\circ$ or 45°. The blue (orange) lines denote the component of SHG response parallel (I_p)(prependicular (I_v)) to the polarization $E(\omega)$ of the incident light 1530 nm.

4 The second-harmonic generation of monolayer MoS_2 and $MoSe_2$

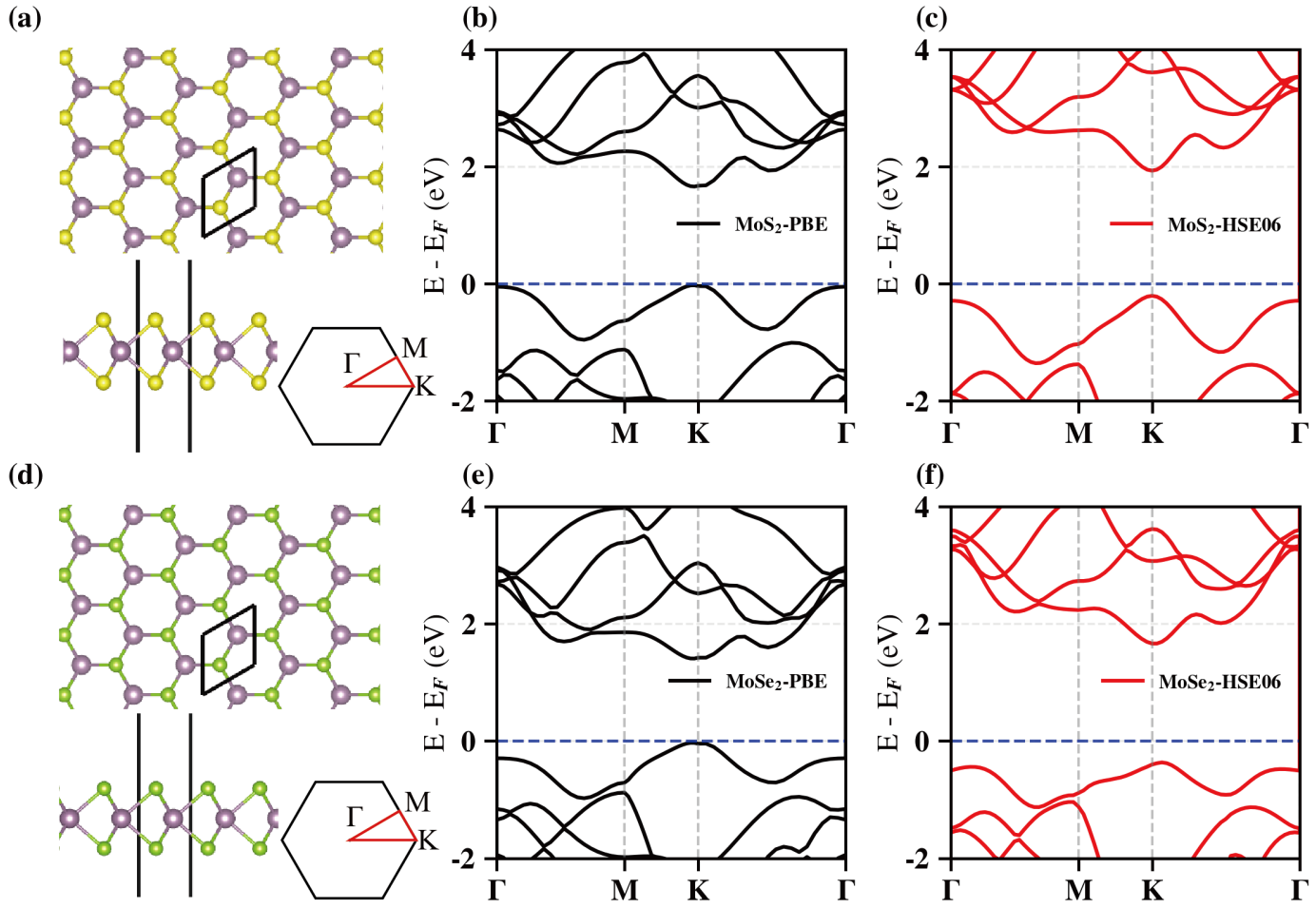

Fig. S15 Top (top) and side (bottom left) views of the atomic structures and first Brillouin zones (bottom right) of monolayer MoS_2 (a) and $MoSe_2$ (d). Electronic structures calculated by PBE (black lines) and HSE06 (red lines) for monolayer MoS_2 (b, c) and $MoSe_2$ (e, f). The Fermi energy level has been set as zero.

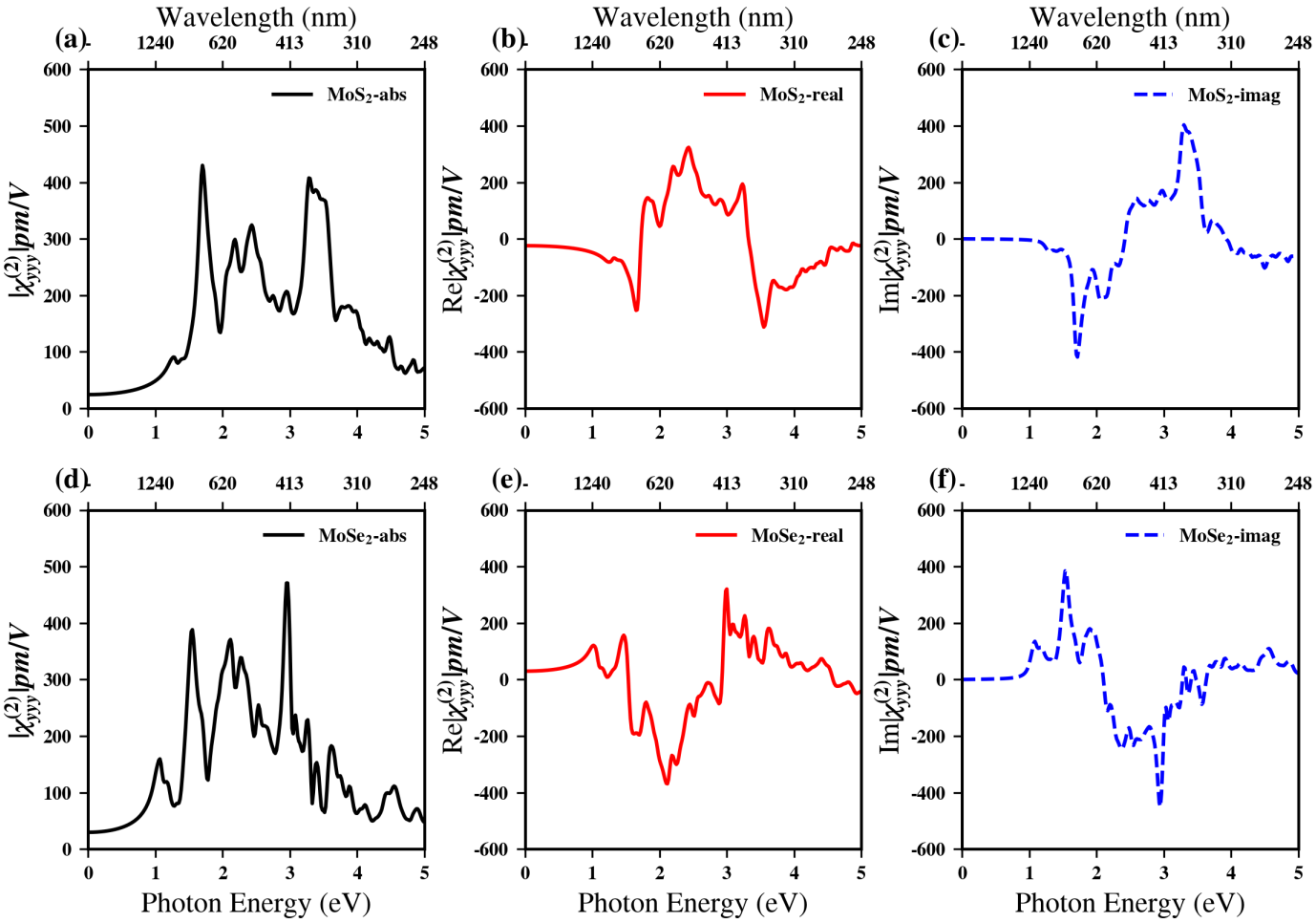

Fig. S16 The non-zero absolute (a; black line), real (b; red line) and imaginary (c; blue line) parts of the independent component $\chi^{(2)}_{yyy}$ of the SHG susceptibility of monolayer MoS_2. Similarly, the non-zero absolute (d), real (e) and imaginary (f) parts of the SHG susceptibility of monolayer $MoSe_2$.

Monolayer MoS_2 and $MoSe_2$ have been calculated using the same method, as shown in Fig. S16. Over 100 conduction bands have been used to obtain converged SHG susceptibility tensors. The peak of the absolute value of the $\chi^{(2)}_{yyy}$ tensor component for monolayer MoS_2 reaches 429.95 pm/V at a wavelength of 729 nm (1.70 eV) and 407.64 pm/V at 378 nm (3.28 eV). The corresponding peaks for monolayer $MoSe_2$ reach 388.11 pm/V at 800 nm (1.55 eV), 362.12 pm/V at 582 nm (2.13 eV) and 470.74 pm/V at 420 nm (2.95 eV). It can be seen that the response intensities of the two materials are comparable, which is consistent with experimental conclusions.[15] The peaks observed in experiments have also been reproduced in our calculations (MoS_2 about 45 pm/V at approximately 700 nm, $MoSe_2$ about 50 pm/V at approximately 800 nm). Theoretical values are often larger than experimental values. The main reasons are that the experimental laser wavelength is often not exactly at the position of the maximum SHG response, as well as interference effects such as the influence of layer number and substrate, and the attenuation of light intensity by lenses. In addition, uncertainties also exist in experimental conclusions obtained relatively by taking quartz as the reference standard.

5 The second-harmonic generation of bulk $KTiOPO_4$

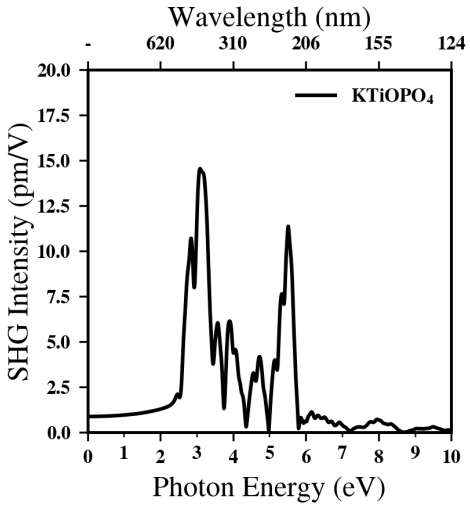

Fig. S17 SHG susceptibility spectrum of bulk $KTiOPO_4$.

Notes and references

1 W. Kohn and L. J. Sham, *Physical review*, 1965, **140**, A1133.

2 G. Kresse and J. Furthmüller, *Physical review B*, 1996, **54**, 11169.

3 P. E. Blöchl, *Physical review B*, 1994, **50**, 17953.

4 J. P. Perdew, K. Burke and M. Ernzerhof, *Physical review letters*, 1996, **77**, 3865.

5 D. C. Langreth and M. Mehl, *Physical Review B*, 1983, **28**, 1809.

6 J. Heyd, G. E. Scuseria and M. Ernzerhof, *The Journal of chemical physics*, 2003, **118**, 8207–8215.

7 R. De L. Kronig, *Journal of the Optical Society of America*, 1926, **12**, 547–557.

8 H. A. Kramers, *La diffusion de la lumiere par les atomes*, 1928.

9 J. Sipe and E. Ghahramani, *Physical Review B*, 1993, **48**, 11705.

10 J. Sipe and A. Shkrebtii, *Physical Review B*, 2000, **61**, 5337.

11 S. N. Rashkeev, W. R. Lambrecht and B. Segall, *Physical Review B*, 1998, **57**, 3905.

12 S. Sharma, J. K. Dewhurst and C. Ambrosch-Draxl, *Physical Review B*, 2003, **67**, 165332.

13 J. L. Hughes and J. Sipe, *Physical Review B*, 1996, **53**, 10751.

14 Z. H. Levine and D. C. Allan, *Physical review letters*, 1991, **66**, 41.

15 C. T. Le, D. J. Clark, F. Ullah, V. Senthilkumar, J. I. Jang, Y. Sim, M.-J. Seong, K.-H. Chung, H. Park and Y. S. Kim, *Annalen der Physik*, 2016, **528**, 551–559.